

## Dendrite-free, interfacially compatible $\text{Na}_2\text{ZrCl}_6$ composite halide solid-state electrolyte for solid state sodium-ion batteries

Hualing Tian,<sup>[a]</sup> Jiajia Li,<sup>[a]</sup> Yanjun Cai,<sup>\*[a]</sup> Xiang Yao,<sup>[a]</sup> Zhi Su<sup>\*[a, b]</sup>

<sup>a</sup> College of Chemistry and Chemical Engineering, Xinjiang Key Laboratory of Energy Storage and Photoelectrolytic Materials, Xinjiang Normal University,

Urumqi, 830054, Xinjiang, P. R. China. E-mail: cyjxsf@yeah.net,

suzhi@xju.edu.cn

<sup>b</sup> Xinjiang University, Urumqi 830017, Xinjiang, P.R. China

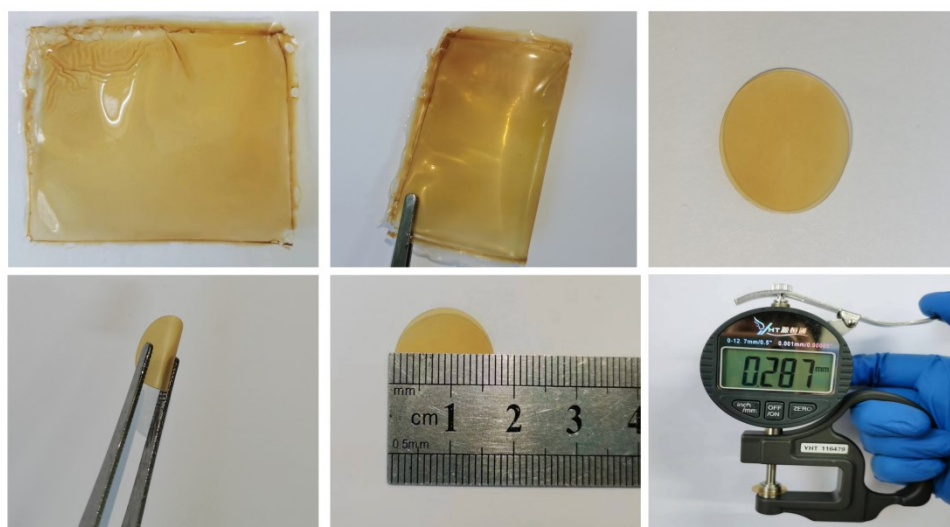


Fig.S1 the optical image of  $\text{Na}_2\text{ZrCl}_6$ -PAN composite solid electrolyte



Fig. S2 thermal stability test of  $\text{Na}_2\text{ZrCl}_6$ -PAN composite solid electrolyte

Table S1 Crystallographic data and powder XRD Rietveld refinement results for Na<sub>2</sub>ZrCl<sub>6</sub>

Space group		$\bar{P}3m1$ (no.164)			
Lattice Parameter, Volume		a = 11.40680Å c = 6.24280Å			
		V = 703.457306 Å <sup>3</sup>			
Atom	Wyckoff site	x	y	z	Occupancy
Na	6g	0.3892	0	0	1.0
Zr1	1a	0	0	0	1.0
Zr2	2d	0.33333	0.66667	0.52690	1.0
Cl1	6i	0.08333	0.91667	0.71250	1.0
Cl2	6i	0.20695	0.79310	0.21710	1.0
Cl3	6i	0.42050	0.57950	0.69820	1.0

Rwp = 5.2 Rexp = 3.48 GOF = 1.4943

The ionic conductivity of the SE was determined by employing assembled stainless steel|SEs|stainless steel (stainless steel SS) symmetric cells and conducting electrochemical impedance spectroscopy (EIS) within a frequency range of 0.1 Hz–10<sup>5</sup> Hz at a temperature range of 30–80 °C. The ionic conductivity of a solid electrolyte is calculated using Eq. (S1):

$$\sigma = d/RS \quad (S1)$$

where  $d$  is the electrolytes thickness and  $S$  is the area ( $R = 16$  mm).  $R$  is the resistance.

The activation energies ( $E_a$ ) of the electrolytes were obtained via the Arrhenius equation, Eq. (S2), as follows:

$$\sigma = A \exp(-E_a/K_B T) \quad (S2)$$

where  $A$  refers to a pre-exponential factor and  $T$  (K) is the experimental temperature. The Na|SEs|Na symmetric cells were assembled using a combination of the time-current method and alternating current impedance (AC) to obtain the sodium transfer number ( $t_{Na^+}$ ). It was calculated via Eq. (S3):

$$t_{Na^+} = I_s(\Delta V - I_0 R_0) / I_0(\Delta V - I_s R_s) \quad (S3)$$

where  $I_0$  and  $R_0$  are the initial current and resistance, respectively;  $I_s$  and  $R_s$  are  $I_s$  and  $R_s$  are the post-polarisation current and resistance, respectively; and  $\Delta V$  is the polarisation voltage (10 mV).

The relaxation time distribution technique (DRT) is an experimental method based on EIS that enables the determination of the relaxation time distribution in a material through the measurement of the frequency response of an electrochemical system via Eq. (S4):

$$Z_{DRT} = R_{\infty} + \int_0^{\infty} r(\ln\tau) / (1 + i 2\pi f\tau) d\ln\tau \quad (S4)$$

where  $\tau$  is the relaxation characteristic time and  $r(\ln\tau)$  is the relaxation characteristic time distribution function. The peak area is indicative of the resistance exhibited by the corresponding process

### Computational details

All of the calculations are performed in the framework of the spin-polarized density functional theory with the projector augmented plane-wave method, as implemented in the Vienna ab initio simulation package (VASP). The generalized gradient approximation (GGA) proposed by Perdew, Burke, and Ernzerhof (PBE) is selected for the exchange-correlation potential. The long-range van der Waals interaction is described by the DFT-D3 approach. The cut-off energy for plane wave is set to 480 eV. The energy criterion is set to 10<sup>-5</sup> eV in iterative solution of the Kohn-Sham equation. All the structures are relaxed until the residual forces on the atoms have declined to less than 0.02 eV/Å. Data analysis and visualization are carried out with the help of VASPKIT code and VESTA. To avoid interlaminar interactions, a vacuum spacing of 20 Å is applied perpendicular to the slab.

The diffusion barrier at different adsorption sites were explored by using the Nudge Elastic Band (CI-NEB) method.

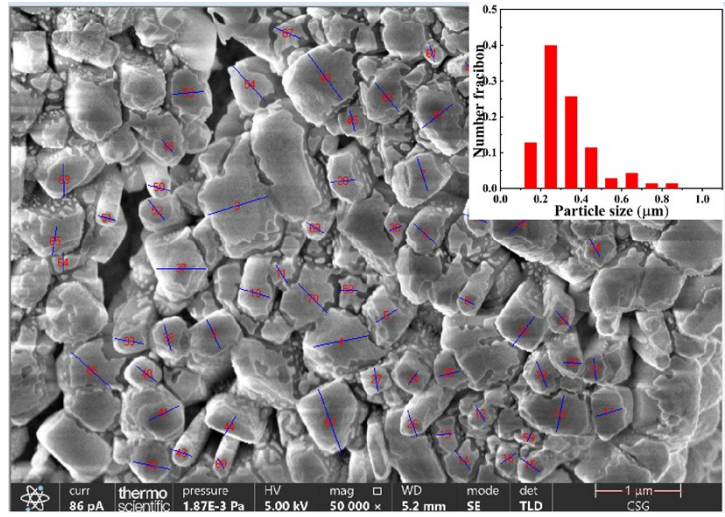


Fig. S3 SEM images of the as-prepared  $\text{Na}_2\text{ZrCl}_6$  materials the insets show the corresponding particle size distributions.

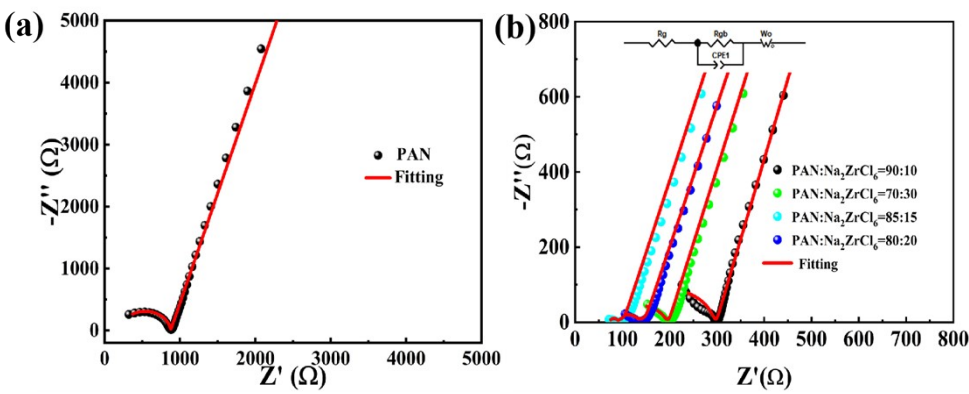


Fig. S4 AC impedance spectrum diagram at 30 °C (a) PAN SE, (b) different  $\text{Na}_2\text{ZrCl}_6$ -to-PAN ratios.

Table S2 Ionic conductivity of different  $\text{Na}_2\text{ZrCl}_6$ -to-PAN ratios SE

ratios	d(cm)	$R_g(\Omega)$	$R_{gb}(\Omega)$	R( $\Omega$ )	$(R_g)(\text{Scm}^{-1})$	$\sigma(R_{gb})(\text{Scm}^{-1})$	$\sigma(R)(\text{Scm}^{-1})$
0	$3.13 \times 10^{-2}$	320	550	870	$4.89 \times 10^{-5}$	$3.09 \times 10^{-5}$	$1.79 \times 10^{-5}$
90:10	$3.20 \times 10^{-2}$	107	190	297	$1.48 \times 10^{-4}$	$8.42 \times 10^{-5}$	$5.41 \times 10^{-5}$
85:15	$2.36 \times 10^{-2}$	65	32	97	$1.81 \times 10^{-4}$	$3.67 \times 10^{-4}$	$1.21 \times 10^{-4}$
80:20	$3.05 \times 10^{-2}$	78	52	130	$1.95 \times 10^{-4}$	$2.93 \times 10^{-4}$	$1.17 \times 10^{-4}$
70:30	$3.10 \times 10^{-2}$	93	106	199	$1.67 \times 10^{-4}$	$1.46 \times 10^{-4}$	$7.78 \times 10^{-5}$

$R = R_g + R_{gb}$ ,  $R_g$  is intra-grain and  $R_{gb}$  inter-grain.

As shown in Fig. S4(a) and table S2, the total ionic conductivity of PAN SE was  $1.79 \times 10^{-5} \text{ S cm}^{-1}$  at 30 °C. The predominant occurrence of ion transport has been observed within the amorphous region. The high crystallinity of PAN has been shown to decrease the proportion of the amorphous region, thereby leading to a subsequent reduction in conductivity. A composite of PAN with inorganic fast ionic conductors has been shown to significantly increase electrical conductivity. The ionic conductivity of  $\text{Na}_2\text{ZrCl}_6$ -PAN SE with different ratios has been demonstrated to exceed that of PAN SE. As illustrated in Fig. S4(b), the ionic conductivity of various SE with different  $\text{Na}_2\text{ZrCl}_6$ -to-PAN ratios. The highest levels of ionic conductivity were observed when the mass ratio of

PAN:Na<sub>2</sub>ZrCl<sub>6</sub> was 85:15. The introduction of Na<sub>2</sub>ZrCl<sub>6</sub> led to a reduction in the crystallinity of the PAN polymer, an increase in the proportion of amorphous regions, and an enhancement in the polymer block motion. These changes collectively contributed to an improvement in the ionic conductivity of the composite solid-state electrolyte. The introduction of Na<sub>2</sub>ZrCl<sub>6</sub> has been shown to form additional sodium ion transport channels and promote sodium ion migration. The incorporation of inorganic fillers into a composite electrolyte has been shown to have a substantial impact on its performance. At a 10% addition rate of Na<sub>2</sub>ZrCl<sub>6</sub>, the formation of continuous ion transport channels is impeded, thereby hindering the enhancement of the composite solid electrolyte's ionic conductivity. The presence of 15% of Na<sub>2</sub>ZrCl<sub>6</sub> in the electrolyte results in the formation of uniformly distributed ion transport channels, leading to a substantial enhancement in ionic conductivity. Furthermore, when the amount of Na<sub>2</sub>ZrCl<sub>6</sub> increases to 20% or 30%, the result is the formation of uniformly distributed ion transport channels, which also leads to a significant increase in ionic conductivity. Furthermore, the addition of excessive quantities of Na<sub>2</sub>ZrCl<sub>6</sub> has been observed to result in a decline in the flexibility of the composite electrolyte, which is susceptible to brittle cracking.

Table S3 Ionic conductivity of Na<sub>2</sub>ZrCl<sub>6</sub>-PAN SE

T(°C)	d (cm)	R <sub>g</sub> (Ω)	R <sub>gb</sub> (Ω)	R (Ω)	σ (R <sub>g</sub> )(S cm <sup>-1</sup> )	σ (R <sub>gb</sub> )(S cm <sup>-1</sup> )	σ (R)(S cm <sup>-1</sup> )
30	2.36×10 <sup>-2</sup>	65	32	97	1.81×10 <sup>-4</sup>	3.67×10 <sup>-4</sup>	1.21×10 <sup>-4</sup>
40	2.36×10 <sup>-2</sup>	60	30	90	1.96×10 <sup>-4</sup>	3.92×10 <sup>-4</sup>	1.31×10 <sup>-4</sup>
50	2.36×10 <sup>-2</sup>	56	15	71	2.10×10 <sup>-4</sup>	7.83×10 <sup>-4</sup>	1.65×10 <sup>-4</sup>
60	2.36×10 <sup>-2</sup>	51	12	63	2.30×10 <sup>-4</sup>	9.79×10 <sup>-4</sup>	1.87×10 <sup>-4</sup>
70	2.36×10 <sup>-2</sup>	40	7	47	2.94×10 <sup>-4</sup>	1.68×10 <sup>-3</sup>	2.50×10 <sup>-4</sup>
80	2.36×10 <sup>-2</sup>	30	1	31	3.92×10 <sup>-4</sup>	1.18×10 <sup>-2</sup>	3.79×10 <sup>-4</sup>

R= R<sub>g</sub>+R<sub>gb</sub>, R<sub>g</sub> is intra-grain and R<sub>gb</sub> inter-grain.

Table S4 Halide Solid State Electrolyte Performance Comparison

SSEs	Stable phase	Synthesis method	ionic conductivity(S cm <sup>-1</sup> )	reference
Na <sub>2</sub> ZrCl <sub>6</sub>	P $\bar{3}$ m1	mechanochemical method	1.8×10 <sup>-5</sup> (30°C)	[1]
Na <sub>2.25</sub> Y <sub>0.25</sub> Zr <sub>0.75</sub> Cl <sub>6</sub>	P2 <sub>1</sub> /n	mechanochemical method	1.7×10 <sup>-3</sup> (RT)	[2]
NaAlCl <sub>4</sub>	C2/m	solid phase	3.9×10 <sup>-6</sup> (30 °C)	[3]
Na <sub>3-x</sub> Y <sub>1-x</sub> Zr <sub>x</sub> Cl <sub>6</sub>	C2/m	mechanochemical method	6.6×10 <sup>-5</sup> (RT)	[4]
P6 <sub>3</sub> -Na <sub>3</sub> Y <sub>2</sub> Cl <sub>9</sub>	P321	mechanochemical method	1.0×10 <sup>-4</sup> (RT)	[5]
Na <sub>3-x</sub> Er <sub>1-x</sub> Zr <sub>x</sub> Cl <sub>6</sub>	P2 <sub>1</sub> /n	mechanochemical method	3.5×10 <sup>-5</sup> (RT)	[6]
NaTaCl <sub>6</sub>	P21/n	mechanochemical method	4×10 <sup>-3</sup> (RT)	[7]
Na <sub>2.5</sub> Cr <sub>0.5</sub> Zr <sub>0.5</sub> Cl <sub>6</sub>	Fm-3m	mechanochemical method	1×10 <sup>-4</sup> (RT)	[8]
Na <sub>2</sub> ZrCl <sub>6</sub> -PAN	P $\bar{3}$ m1	mechanochemical method	1.21×10 <sup>-4</sup> (30°C)	<b>This work</b>

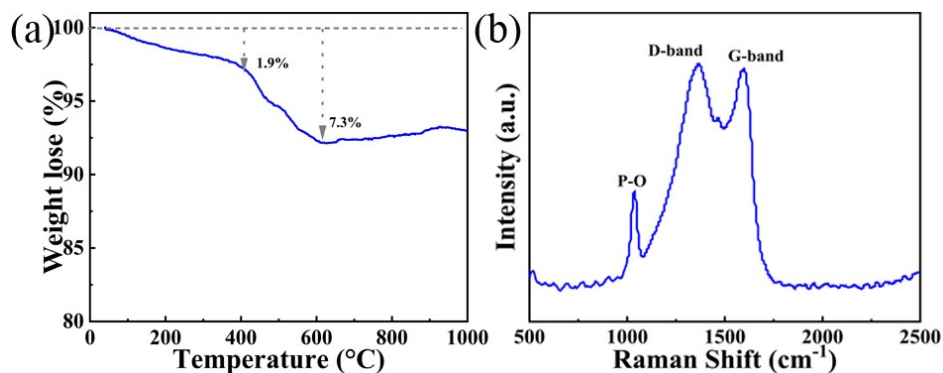


Fig. S5 NVP of the material (a) thermogravimetric curve, (b) Raman mapping.

The TGA technique was used for sample characterization, and the experiments were conducted in the temperature range spanning 30°C to 1000 °C to determine the carbon content in the NVP/C-25 min sample. In Fig. S5(a), adsorbed water molecules evaporate at 400 °C, resulting in initial weight loss. Carbon present in the material was removed by the oxidation of carbon in air in the presence of oxygen. This results in a rapid decrease in weight in the temperature range of 300-600 °C. The experimental results show that the carbon content in the NVP/C-25 min sample is approximately 5.4% of the total weight.

Raman spectral profiles recorded for NVP/C-25 min nanocomposites are displayed in Fig. S5(b). The profiles recorded for the NVP/C-25 min sample exhibited the presence of two distinct peaks at  $\sim 1344$  and  $\sim 1588$   $\text{cm}^{-1}$ , corresponding to the disorder-induced D-band and the G-band of carbon, respectively. Another small peak corresponding to  $\text{PO}_4$  appeared at  $\sim 1060$   $\text{cm}^{-1}$ . In addition, it is reported that carbon with a lower  $I_D/I_G$  ratio contains more graphite crystals than disordered carbon. Typically, an  $I_D/I_G$  value of  $<1$  indicates good electrical conductivity. We recorded the  $I_D/I_G$  value to be 1.04, and this value indicates that graphitization of residual carbon occurs in the synthetic material under reduced conditions at a microwave power of 600 W and radiation time of 25 min.

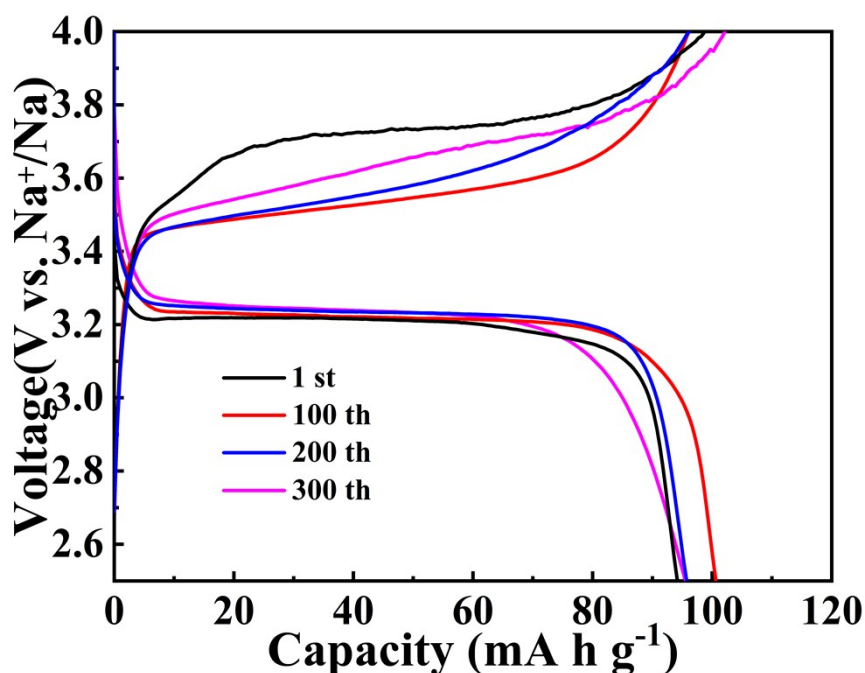


Fig. S6 Na|Na<sub>2</sub>ZrCl<sub>6</sub>-PANINVP ASSIBs ocharge/discharge curves at 0.5 C

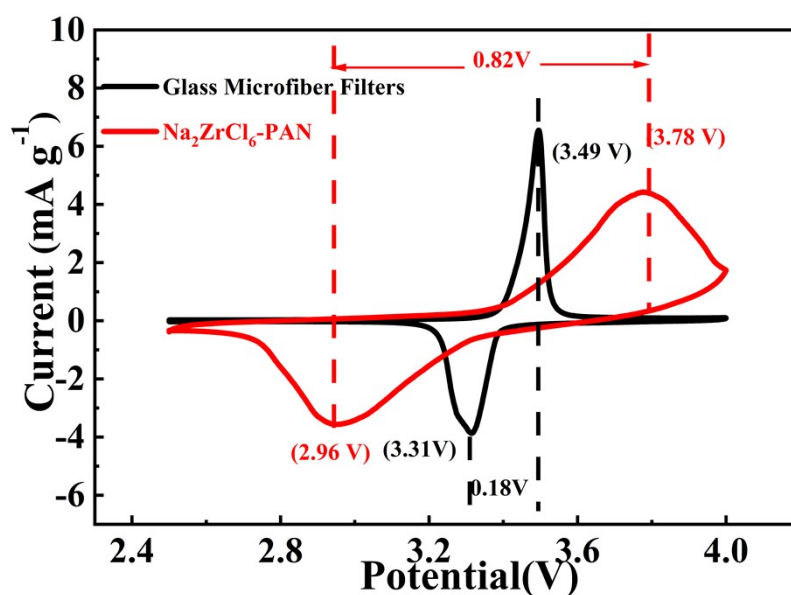


Fig.S7 Na<sub>2</sub>ZrCl<sub>6</sub>-PANINVP ASSIBs CV curves

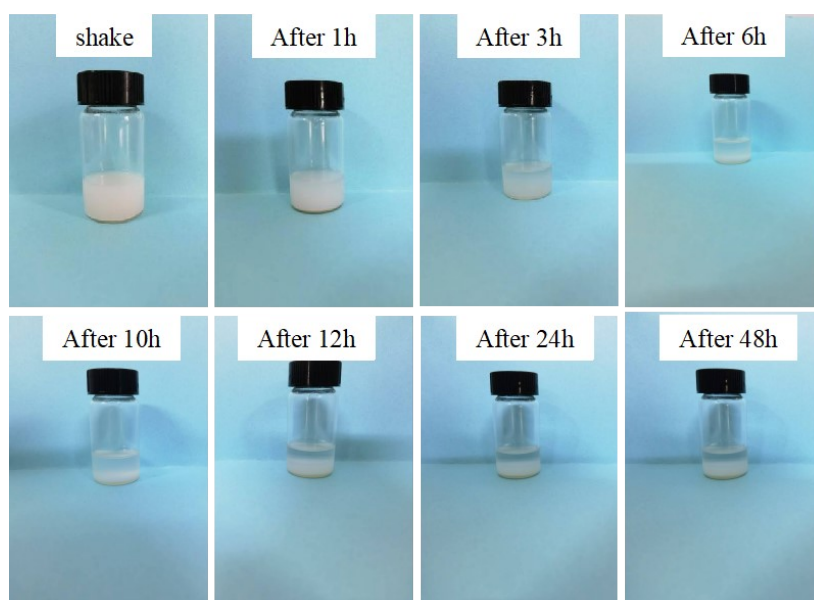


Fig. S8 Solubility experiments of Na<sub>2</sub>ZrCl<sub>6</sub> in electrolytes

Fig. S8 shows the solubility test of Na<sub>2</sub>ZrCl<sub>6</sub> in the electrolyte solution. The Na<sub>2</sub>ZrCl<sub>6</sub> powder was introduced into 10 mL of electrolyte (1 M NaClO<sub>4</sub> in DMC:EC = 1:1 vol%, with 5% FEC), following which the solution was subjected to agitation to induce a turbid state. After 1 h of set aside, the material exhibited substantial delamination. Following a period of 6 h during which the mixture stood undisturbed, a complete separation of the solid and liquid phases had occurred, with the formation of a Na<sub>2</sub>ZrCl<sub>6</sub> precipitate occurring at the base of the mixture. Experiments involving liquid absorption rate demonstrated that Na<sub>2</sub>ZrCl<sub>6</sub>-PAN SE exhibited a low liquid absorption rate. The mixed solution exhibited negligible change when observed continuously over the course of 48 h. Furthermore, solubility experiments demonstrated that Na<sub>2</sub>ZrCl<sub>6</sub> is not soluble in the electrolyte, indicating that the solvent heat is low.

Na<sub>2</sub>ZrCl<sub>6</sub> is a tripartite crystal system, with a crystal structure that features layer stacking and high lattice energy. Due to its high lattice energy, Na<sub>2</sub>ZrCl<sub>6</sub> exhibits low solubility in organic solvents. On the other hand, the presence of a highly charged metal cation, Zr<sup>4+</sup>, renders Na<sub>2</sub>ZrCl<sub>6</sub> more stable and less soluble. In order to enhance the interfacial wettability of the composite solid electrolyte and the electrode material, the Na<sub>2</sub>ZrCl<sub>6</sub>-PAN SE was immersed in the electrolyte (1 M NaClO<sub>4</sub> in DMC:EC = 1:1 vol%, with 5% FEC) for 10 min prior to assembling the cell. To evaluate the liquid absorption rate of the Na<sub>2</sub>ZrCl<sub>6</sub>-PAN SE in the electrolyte solution, ten

sets of Na<sub>2</sub>ZrCl<sub>6</sub>-PAN SE was selected and immersed in the electrolyte for 10 min, yielding the following results. The average mass of the composite electrolyte before immersion m<sub>1</sub>= 0.115 g. The average mass of the composite solid electrolyte after 10 min m<sub>2</sub>=0.136 g, Δm=21 mg, indicating that the electrolyte had been absorbed. The calculation of the liquid absorption rate of the composite solid electrolyte is by the Eq. (S5):

$$\text{absorbing liquid ratio(\%)} = W_{\text{wet}} - W_{\text{dry}} / W_{\text{dry}} \times 100 \quad (\text{S5})$$

$W_{\text{dry}}$  and  $W_{\text{wet}}$  are the masses of dry and wet films respectively.

Calculated from Eq. 1, Na<sub>2</sub>ZrCl<sub>6</sub>-PAN SE with 18% liquid absorption. Experiments involving liquid absorption rate demonstrated that Na<sub>2</sub>ZrCl<sub>6</sub>-PAN SE exhibited a low liquid absorption rate.

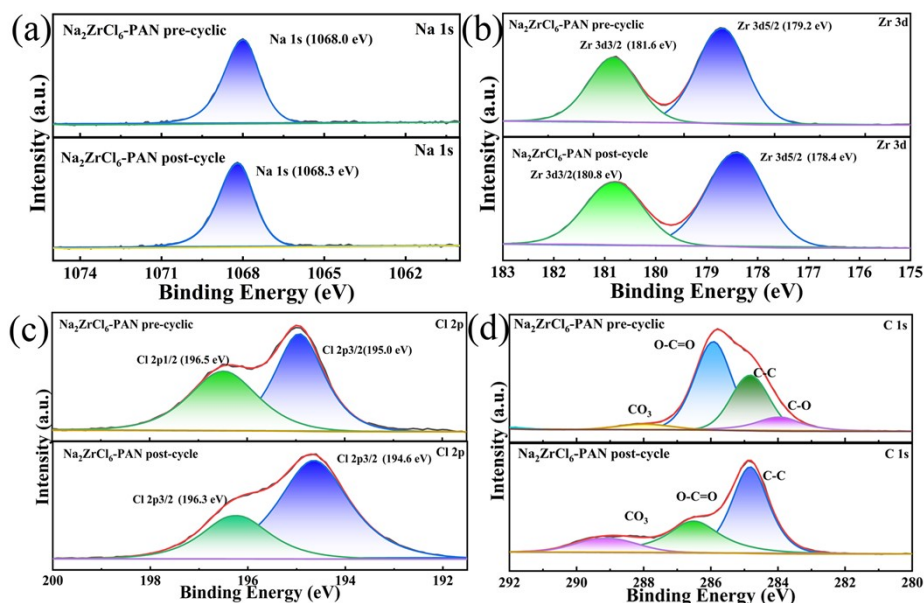


Fig. S9 XPS of Na<sub>2</sub>ZrCl<sub>6</sub>-PAN composite electrolyte before and after electrochemical cycling (a) Na 1s, (b) Zr 3d, (c) Cl 2p, (d) C 1s.

In order to investigate the stability of the electrolyte/Na interface, XPS tests were performed on Na<sub>2</sub>ZrCl<sub>6</sub>-PAN SE before and after electrochemical cycling of Na|Na symmetric cell. As illustrated in Figure S8 (a-c), the XPS spectra of Na 1s, Zr 3d, and Cl 2p were examined before and after electrochemical cycling. Prior to and following the electrochemical cycling process, Na 1s was located at 1068 eV, corresponding to Na<sup>+</sup> 1s, no substantial displacement was observed in this region. The Zr 3d of Na<sub>2</sub>ZrCl<sub>6</sub> is located at 181.6 eV and 179.2 eV, corresponding to Zr<sup>4+</sup> 3d 3/2 and Zr<sup>4+</sup> 3d 5/2, respectively. The Cl 2p was located at 196.5 eV and 195.0 eV before and after the electrochemical reaction, corresponding to Cl<sup>-</sup> 2p 1/2 and Cl<sup>-</sup> 2p 3/2, respectively. The Na 1s, Zr 3d, and Cl 2p XPS energies exhibited minimal alterations before and after the electrochemical reaction, indicating that the structure of Na<sub>2</sub>ZrCl<sub>6</sub> remained stable during and after the electrochemical cycling process and that no chemical reaction transpired. As illustrated in Fig. S8(d), the XPS spectra of C 1s were examined before and after the electrochemical reaction. The elevated concentration of CO<sub>3</sub><sup>2-</sup> on the surface of Na<sub>2</sub>ZrCl<sub>6</sub>-PAN SE following electrochemical cycling undergoes a reaction with Na<sup>+</sup> to yield Na<sub>2</sub>CO<sub>3</sub>. The SEI film generated at the electrolyte/Na interface has been demonstrated to facilitate the cycling stability and safety of Na|Na<sub>2</sub>ZrCl<sub>6</sub>-PANINVP SSIBs. However, over time, an increasing amount of Na<sub>2</sub>CO<sub>3</sub> is generated at the interface, which can result in an enhancement of interfacial impedance.

## References

- [1] H. Kwak, J. Lyoo, J. Park, Y. Han, R. Asakura, A. Remhof, C. Battaglia, H. Kim, S. Hong, Y. Jung, *Energy Storage Materials*, 2021, **37**, 47-57.
- [2] E. Sebti, J. Qi, P. Richardson, P. Ridley, E. Wu, S. Banerjee, R. Giovine, *J. Mater. Chem. A*, 2022, **10**, 21565-21575.
- [3] E. Wu, S. Banerjee, H. Tang, P. Richardson, J. Doux, J. Qi, Z. Zhu, A. Grenier, Y. Li, E. Zhao, G. Deysher, H. Nguyen, R. Stephens, G. Verbist, K. W. Chapman, R. Clément, A. Banerjee, Y. Meng, S. Ong, *Nat. Commun.*, 10.1038/s41467-021-21488-7.
- [4] J. Park, J. Son, W. Ko, J. Kim, Y. Choi, H. Kim, H. Kwak, D. Seo, J. Kim, Y. Jung, *ACS Energy Lett.*, 2022, **7**, 3293-3303.
- [5] J. Xu, Y. Wang, S. Wu, Q. Yang, X. Fu, R. Xiao, H. Li, *ACS Appl. Mater. Interfaces*, 2023, **15**, 21086-21097.
- [6] R. Schlem, A. Banik, M. Eckardt, M. Zobel, W. Zeier, *ACS Appl. Energy Mater.*, 2020, **3**, 10164-10175.
- [7] Y. Hu, J. Fu, X. Lin, J. Xu, J. Luo, F. Zhao, Y. Liu, W. Li, J. Kim, H. Su, X. Hao, H. Ren, M. Yang, Y. Huang, X. Sun, *Matter*, DOI:10.1016/j.matt.2023.12.017.
- [8] L. Wang, Z. Song, X. Lou, Y. Chen, T. Wang, Z. Wang, H. Chen, W. Yin, M. Avdeev, W. Kan, B. Hu, W. Luo, *Small*, 2024, 1-10.